Magnetic states of iron-based two-leg ladder tellurides

Yang Zhang,[1,2] Ling-Fang Lin,[1,2] Adriana Moreo,[1,3] Shuai Dong,[2] and Elbio Dagotto[1,3,*]

[1]*Department of Physics and Astronomy, University of Tennessee, Knoxville, Tennessee 37996, USA*

[2]*School of Physics, Southeast University, Nanjing 211189, China*

[3]*Materials Science and Technology Division, Oak Ridge National Laboratory, Oak Ridge, Tennessee 37831, USA*

(Received 27 August 2019; revised manuscript received 16 October 2019; published 25 November 2019)

The recent discovery of superconductivity at high pressure in the two-leg ladder compounds $BaFe_2X_3$ (X= S, Se) started the novel field of quasi-one-dimensional iron-based superconductors. In this paper, we use density functional theory (DFT) to predict that the previously barely explored ladder compound $RbFe_2Te_3$ should be magnetic with a CX-type arrangement involving ferromagnetic rungs and antiferromagnetic legs, at the realistic density of $n = 5.5$ electrons per iron. The magnetic state similarity with $BaFe_2S_3$ suggests that $RbFe_2Te_3$ could also become superconducting under pressure. Moreover, at $n = 6.0$ our DFT phase diagrams (with and without lattice tetramerization) reveal that the stable magnetic states could be either a 2×2 magnetic block-type, as for X= Se, or a previously never observed before CY-type state, with ferromagnetic legs and antiferromagnetic rungs. In the Te-based studies, electrons are more localized than in S, implying that the degree of electronic correlation is enhanced for the Te case.

DOI: 10.1103/PhysRevB.100.184419

I. INTRODUCTION

Although the first high critical temperature iron-based superconductors were discovered more than a decade ago, the origin of their pairing mechanism is still highly debated and the topic remains one of the most important open problems in condensed matter physics [1–4]. It is widely believed that the crystal structure, magnetic properties, and the degree of electronic correlation are all fundamental aspects to clarify the physics of these materials [2,5–7]. For the vast majority of initially reported iron-based superconductors, the crystal structures consisted of slightly distorted two-dimensional (2D) iron square lattices made of FeX_4 tetrahedra (X = pnictides or chalcogens) [6,8,9]. The electronic correlation effects can not be neglected [4], causing many novel physical features, such as Fermi surfaces without hole pockets, complex magnetic spin orders, as well as orbital selective Mott states [2,4].

Recently, the discovery of superconductivity in the so-called 123-type compounds $BaFe_2X_3$ (X= S/Se) opened a new branch of research in iron-based superconductors [10,11]. Different from the 2D iron square lattice arrangement, the 123-type iron chalcogenides display a dominant quasi-one-dimensional two-leg ladder crystal structure that has been much analyzed [12–17]. These recent developments resemble the discovery in the 1990's of superconductivity in Cu-oxide ladders [18–20] that also opened a fertile area of research.

At the equilibrium structure without external pressure, $BaFe_2S_3$ displays CX stripe antiferromagnetic (AFM) order, AFM along the legs and ferromagnetic (FM) along the rungs, below 120 K with a magnetic moment $\sim 1.2\,\mu_B$/Fe [10,21]. This magnetic moment is smaller than the theoretical maximum value of $4\,\mu_B$/Fe, obtained by considering the high-spin $S = 2$ configuration and the electronic density $n = 6.0$ for $BaFe_2S_3$. Superconductivity was observed at $P \sim 11$ GPa with the highest critical temperature T_c being 24 K [10,22]. Since then, several experimental and theoretical studies have followed [23–27]. Above 10 GPa, a metal-insulator transition (MIT) and associated first-order magnetic phase transition were recently observed for $BaFe_2S_3$ [28,29]. One possible explanation is that pressure changes the bandwidth of these materials, thus altering the degree of correlation [10,11]. An alternative, based on model calculations, is that high pressure could change the Fe electronic density, effectively doping the two-leg ladders. In fact, calculations based on the density matrix renormalization group [30] observed clear tendencies to form Cooper pairs at intermediate Hubbard coupling strengths upon light doping. Similar self-doping effects under pressure were also obtained using DFT calculations [28].

$BaFe_2Se_3$ is another recently discovered superconducting ladder under high pressure [11]. Without external pressure, $BaFe_2Se_3$ is an AFM Mott insulator and displays an exotic block-type magnetic order below $\sim$256 K, with a robust local magnetic moment $\sim 2.8\,\mu_B$/Fe [12,13,31,32]. This material is theoretically predicted to be multiferroic [16] and recently confirmed to be polar at high temperature [33]. In particular, $BaFe_2Se_3$ is in an orbital-selective Mott phase (OSMP) according to neutron experiments at ambient pressure [17]. Moreover, there are several other two-leg ladder iron chalcogenides, with almost all the studies focusing on iron sulfides and selenides. For example, KFe_2Se_3 was observed to have a CX-type stripe AFM order [31], similarly as $CsFe_2Se_3$ [21] and $RbFe_2Se_3$ [23]. In particular, the KFe_2S_3 compound was predicted to display a first-order transition under high pressure in our recent work [28].

Considering the columns of pnictogens and chalcogens in the periodic table, the next natural step in iron ladders is to

*Corresponding author: edagotto@utk.edu

 ©2019 American Physical Society

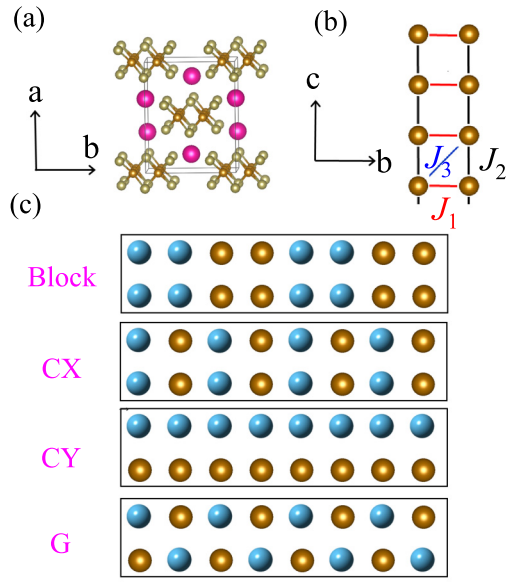

FIG. 1. (a) Schematic crystal structure of $RbFe_2Te_3$ (electronic density $n = 5.5$) with the following convention: pink = Rb; brown = Fe; dark yellow = Te. (b) Sketch of one *Cmcm* ladder. The iron-iron distance is uniform along the legs. (c) Sketch of possible antiferromagnetic magnetic orders in each individual ladder studied here. Spin up and spin down are distinguished by different colored balls.

move one row down and use Sb or Te. However, surprisingly there is virtually no experimental literature available using these elements. For Te, we are only aware of *one* publication many years ago where it was reported that $RbFe_2Te_3$ also favors the *Cmcm* crystal structure [34], similar to $BaFe_2S_3$, where the iron-iron distances are uniform in the nontilting ladder, as shown in Fig. 1. In $RbFe_2Te_3$, the valence of Fe is +2.5 indicating that the realistic density is $n = 5.5$ electrons per iron considering the $4s^2 3d^6$ configuration in the Fe atoms. It is important to remark that there are still no $n = 5.5$ ladders being reported to be superconducting under high pressure.

In this paper, the magnetic properties and electronic structure corresponding to $RbFe_2Te_3$ are studied based on first-principles DFT calculations. The CX-type spin order is predicted to be the most likely magnetic ground state in our $n = 5.5$ DFT phase diagrams. For comparison, for the $n = 6.0$ $BaFe_2Se_3$ compound the 2×2 magnetic block-type state was found to be stable after including lattice tetramerization. In the Te-based compound, we found that electrons are more localized than in S, implying that the degree of electronic correlation is enhanced for the Te case. Future experimental efforts should be devoted to this interesting Te-ladder compound.

II. METHOD

The first-principles DFT calculations used here were performed with the projector augmented-wave (PAW) potentials as implemented in the Vienna *ab initio* simulation package (VASP) code [35,36]. The Perdew-Burke-Ernzerhof (PBE) exchange function was employed [37] and the plane-wave cutoff energy was 500 eV. Since different magnetic configurations have different minimal unit cells, the mesh was appropriately modified for all the candidates to render the k-point densities approximately the same in reciprocal space, i.e., $6 \times 6 \times 8$ for block type and $6 \times 5 \times 10$ for FM type. In addition, we have tested that these k-point meshes already lead to converged energies when compared with denser meshes.

As a first step, we considered the spin-polarized version of the generalized gradient approximation (GGA) potential [37] to study the lattice ground-state properties of bulk $RbFe_2Te_3$. Since the PBE-GGA function is known to give an accurate description of the two-leg ladder systems [28,38,39], we do not consider the effective Hubbard U_{eff}. Both the lattice constants and atomic positions were fully relaxed with different spin configurations until the force on each atom was below 0.005 eV/Å.

To understand magnetism, we adopted the local density approximation (LDA)+U method [40], where the onsite Coulomb interaction U and onsite exchange interaction J were considered. To reduce the computing time required, we just considered the (0, 0, 0) order between ladders with a minimum unit cell to obtain the phase diagram of the $n = 5.5$ and 6.0 ladders. Due to the dominance of the in-ladder magnetic order, the magnetic correlations between ladders can only slightly affect the energies and physical properties.

The generalized LDA + U functional is the following [40,41]:

$$E^{\text{LDA}+U}[\rho^\sigma(r), \{n^\sigma\}] = E^{\text{LSDA}}[\rho^\sigma(r)] + E^U[\{n^\sigma\}] - E_{\text{dc}}[\{n^\sigma\}], \quad (1)$$

where $\rho^\sigma(r)$ is the charge density for electrons with spin projection σ, while $\{n^\sigma\}$ are the elements of the density matrix. Here, the density matrix is defined as

$$n^\sigma_{mm'} = -1/\pi \int^{E_F} \text{Im} G^\sigma_{ilm,ilm'}(E) dE, \quad (2)$$

where i denotes site, l indicates the orbital quantum number, and m the spin number. Note that there is summation for i and l implicit, $G^\sigma_{ilm,ilm'}(E) = \langle ilm\sigma|(E - H)^{-1}|ilm'\sigma\rangle$ are the matrix elements of the Green function matrix in the localized representation, and H is the effective single-electron Hamiltonian. The orbital polarizations are absent in the LSDA first term, and the second term in Eq. (1) can be described by the Hartree-Fock (HF) mean-field theory [40,41]:

$$E^U[\{n\}] = 1/2 \sum_{\{m\},\sigma} \{\langle m, m''|V_{\text{ee}}|m', m'''\rangle n^\sigma_{mm'} n^{-\sigma}_{m''m'''} + (\langle m, m''|V_{\text{ee}}|m', m'''\rangle - \langle m, m''|V_{\text{ee}}|m''', m'\rangle) n^\sigma_{mm'} n^\sigma_{m''m'''}\}, \quad (3)$$

where V_{ee} are the screened Coulomb interactions among nl electrons. The double-counting term (E_{dc}) is described by

$$E_{\text{dc}}[\{n^\sigma\}] = 1/2Un(n-1) - 1/2J[n^\uparrow(n^\uparrow - 1) + n^\downarrow(n^\downarrow - 1)], \quad (4)$$

where $n^\sigma = \text{Tr}(n^\sigma_{mm'})$ and $n = n^\uparrow + n^\downarrow$. U and J are the Coulomb interaction and exchange interaction, respectively. If the density matrix becomes diagonal, the present rotationally invariant method is equivalent to the ordinary LDA + U approach [42].

TABLE I. The optimized lattice constants (Å), local magnetic moments (in μ_B/Fe units) within the default PAW sphere, and band gaps (eV) for the various magnetic configurations, as well as the energy differences (meV/Fe) with respect to the CX configuration taken as the reference of energy. The experimental values (Expt. for short) are also listed for comparison.

	$a/b/c$	M	Gap	Energy
NM	12.665/9.953/5.683	0	0	396
FM	13.164/10.625/5.629	2.64	0	238
CX	12.803/10.233/5.868	2.71	0.39	0
CY	12.622/10.522/5.653	2.43	0	236
G	12.771/10.326/5.795	2.54	0	90
Block	13.008/10.454/5.570	2.45	0	158
Expt.	12.486/10.126/5.921			

III. RESULTS

A. Physical properties of $RbFe_2Te_3$

To find out what magnetic configuration becomes the ground state of $RbFe_2Te_3$, we adopted the spin-polarized method within the GGA potential to fully relax the crystal lattices and atomic position since the PBE-GGA function was widely used in previous DFT calculations of two-leg iron ladder systems [26,28,38,39]. Various possible (in-ladder) magnetic arrangements were imposed on the iron ladders [see Fig. 1(c)], such as nonmagnetic (NM), FM, AFM with FM rungs and AFM legs (CX), AFM with AFM rungs and FM legs (CY), AFM in both rung and leg directions (G), and 2×2 block-AFM (block) [28]. Furthermore, the $(\pi, \pi, 0)$ order between ladders was adopted, as suggested by neutron scattering results [31] for $K_xBa_{1-x}Fe_2Se_3$. Our main results for $RbFe_2Te_3$ are summarized in Table I.

Under ambient conditions, our DFT calculations performed for several magnetic candidates [the tested spin configurations are shown in Fig. 1(c)] indicate that the CX-type magnetic order is the most stable ground state of the ensemble used. For this CX-type state, the calculated local magnetic moment of Fe is about 2.71 μ_B/Fe. It should be noted that it is quite common to overestimate the local magnetic moment when using the spin-polarized method within the GGA potential in calculations of iron-based superconductors [5,28,39], which could be caused by the coexistence of localized Fe spins and itinerant electrons [43]. Another possibility is the existence of strong quantum zero-point fluctuations in this quasi-one-dimensional two-leg ladder system. For comparison, the calculated local magnetic moment for $BaFe_2S_3$ and KFe_2Se_3 are 2.08 μ_B/Fe [28,39] and 2.65 μ_B/Fe [28], respectively, which are larger than the experimental values 1.2 μ_B/Fe and 2.1 μ_B/Fe [10,44]. Hence, it is reasonable to assume that the experimental magnetic moment would be smaller than our calculated value for $RbFe_2Te_3$.

The DFT calculated energy gap corresponding to the CX-type AFM order is about 0.39 eV, which is close to the activation gap reported for $CsFe_2Se_3$ [14]. This calculated gap for $RbFe_2Te_3$ is larger than the experimental value of $BaFe_2S_3$ ~ 0.06–0.07 eV [45]. According to the empirical knowledge gathered on iron ladders, the larger gap indicates that a much higher pressure will be needed in the Te case to achieve an insulator-metal transition, or to suppress magnetism, than in the S or Se cases.

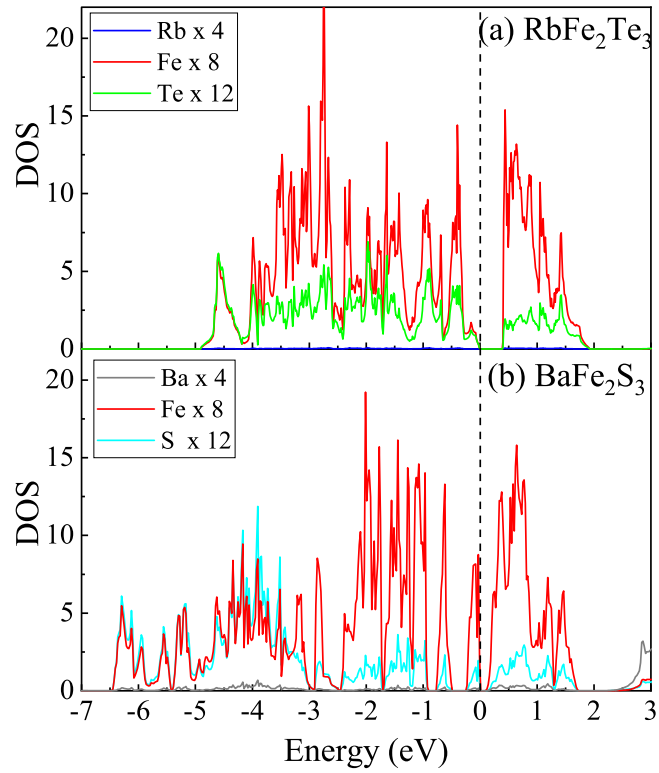

FIG. 2. DOS near the Fermi level using the CX-AFM states $(\pi, \pi, 0)$ for (a) $RbFe_2Te_3$ (at electronic density $n = 5.5$) and $BaFe_2S_3$ (at electronic density $n = 6.0$), respectively. Blue = Rb; black = Ba; red = Fe; green = Te; cyan = S.

Considering the intraladder magnetic order, the magnetism of $RbFe_2Te_3$ could be described by a simple Heisenberg model:

$$H_{\text{spin}} = -J_1 \sum_{\langle i,j \rangle} \mathbf{S}_i \cdot \mathbf{S}_j - J_2 \sum_{[k,l]} \mathbf{S}_k \cdot \mathbf{S}_l - J_3 \sum_{\{m,n\}} \mathbf{S}_m \cdot \mathbf{S}_n, \tag{5}$$

where J_1 and J_2 are the exchange interactions in the rung and leg directions, respectively, while J_3 is the exchange coupling along the plaquette diagonal of iron atoms [Fig. 1(b)]. By fitting the DFT energies of various magnetic states, all the coefficients of this Heisenberg model can be obtained: $S^2J_1 =$ 44.2 meV, $S^2J_2 = -96.1$ meV, and $S^2J_3 = -23.1$ meV, respectively [46]. Similar to two-dimensional magnetic stripe iron superconductors and other two-leg iron ladders [3,23,47], they all display that the magnitude of the FM rung exchange coupling is smaller than the magnitude of the AFM leg coupling.

According to the calculated density of states (DOS) of the CX-type AFM order of $RbFe_2Te_3$ [see Fig. 2(a)], the bands near the Fermi level are mainly contributed by Fe-3d orbitals which are hybridized with Te-5p orbitals. For comparison, we displayed the DOS of the CX-type AFM state of $BaFe_2S_3$ in Fig. 2(b). The bandwidth of the five iron bands of $RbFe_2Te_3$ (~6.8 eV) is smaller than $BaFe_2S_3$ (~8 eV), which indicates that effectively the iron orbitals in $RbFe_2Te_3$ are more

localized than in $BaFe_2S_3$. As remarked below, remember that the Fe-Fe effective hopping is mediated by Te as a bridge, thus iron bandwidths are a consequence of Fe-Te-Fe hoppings. It is interesting that the weight of Fe and Te near the Fermi level are smaller than in the case Fe and S. One possible reason is that $RbFe_2Te_3$ has 0.5 electrons less than $BaFe_2S_3$ per iron ion, resulting in fewer iron states in $RbFe_2Te_3$.

B. Magnetic phase diagrams for two-leg ladders at electronic densities $n = 5.5$ and 6.0

To understand better the magnetic properties of two-leg iron ladders, we used the LDA + U method with the equilibrium structural parameters to compare different spin configurations by changing the onsite Coulomb interaction U and onsite exchange interaction J. Here, to save computing resources, the (0, 0, 0) order between ladders was considered because the in-ladder magnetic coupling is dominant in two-leg iron systems.

Let us start our description of the main results considering the ladder electronic density $n = 5.5$, corresponding to $RbFe_2Te_3$, using periodic boundary conditions, based on the experimental crystal structure [34]. As shown in Fig. 3(a), there is only one magnetic state (CX-type) stable in our phase diagram [except for one anomalous point ($U = 1.5$ eV and $J/U = 0.15$)] even when the Hubbard coupling U and exchange interaction J are varied in a wide range. This clearly indicates that the CX-type order is quite stable in our $n = 5.5$ phase diagram, which is consistent with existing studies of magnetism in $n = 5.5$ iron ladders [10,23,31]. Hence, we arrive to the reasonable conclusion that CX-type AFM is the most likely magnetic ground state of Te-based ladders, and likely other iron ladders with electronic density $n = 5.5$. This CX state of iron ladders can be considered quite similar to the prevalent stripe C-AFM order of iron 2D-layered systems [4,48,49].

To qualitatively describe the Mott insulator of $RbFe_2Te_3$, we calculated the magnetic moment and energy gap by increasing U at the realistic $J/U = 0.25$ [4], as displayed in Fig. 3(b). When U is small, the magnetic moment of iron is zero, all the iron bands overlap, and the system is in a metallic state. By increasing U to a critical value, the spin-up and -down bands split, resulting in the CX-type AFM order while the system is still metallic in a very narrow U range near 1.25 eV. Continuing to increase U, the valence band and the conduction band separate from each other, opening a gap and producing an insulating phase. Our results for $J/U = 0.25$ qualitatively describe the Mott metal-insulator phase transition. In our LDA + U approximation, the Hubbard U splits the the spin up/down near $U = 1.2$ eV, and opens the gap at $U = 1.4$ eV.

Let us consider now the results for ladders with electronic density $n = 6.0$, corresponding to $BaFe_2Se_3$, which experimentally is known to display the exotic 2×2 block-type AFM order [31]. As a first step, we use the crystal structure *without* lattice tetramerization. Here, we adopted the crystal structure based on the *Pnma* phase obtained from neutron experiments [44] which does not consider the magnetic exchange striction effect. The phase diagram that we obtained for $n = 6.0$ iron ladders becomes far richer than at $n = 5.5$,

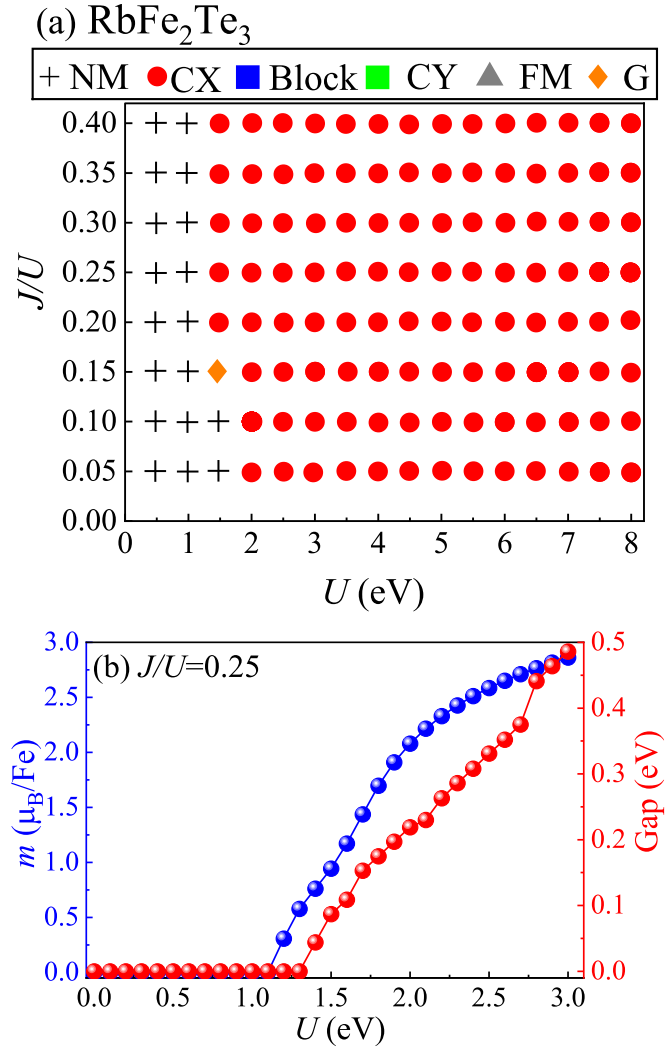

FIG. 3. (a) Phase diagram based on the experimental lattice constants of $RbFe_2Te_3$, employing the LDA + U technique at the electronic density $n = 5.5$. (b) Evolution of local magnetic moments and band gaps of $RbFe_2Te_3$ for the CX-type AFM magnetic state, as a function of U, at $J/U = 0.25$.

as displayed in Fig. 4(a), including five different magnetic states, with a surprising dominance of the CY state, followed by CX with regard to area covered in the phase diagram [50]. Note that here there is only a small region of the block-type order in our DFT phase diagram, although this state is the one found experimentally in Se-based ladders. However, it should be remarked that the energy between block-type and CY-type is less than 10 meV/Fe at $U = 3$ and 3.5 eV. In other regions of our phase diagram, the energy of the block-type remains only slightly higher than the energy of the CY-type. To address better this issue, note that the block-type AFM order naturally brings up the issue of exchange magnetostriction related to a possible lattice tetramerization induced by this block order, which would reduce the overall energy. Hence, the block-type order will likely become more stable than the CY-type in some region by considering the lattice tetramerization. Moreover, according to related DFT calculations and actual experiments [16,33,38], the symmetry of the crystal structure

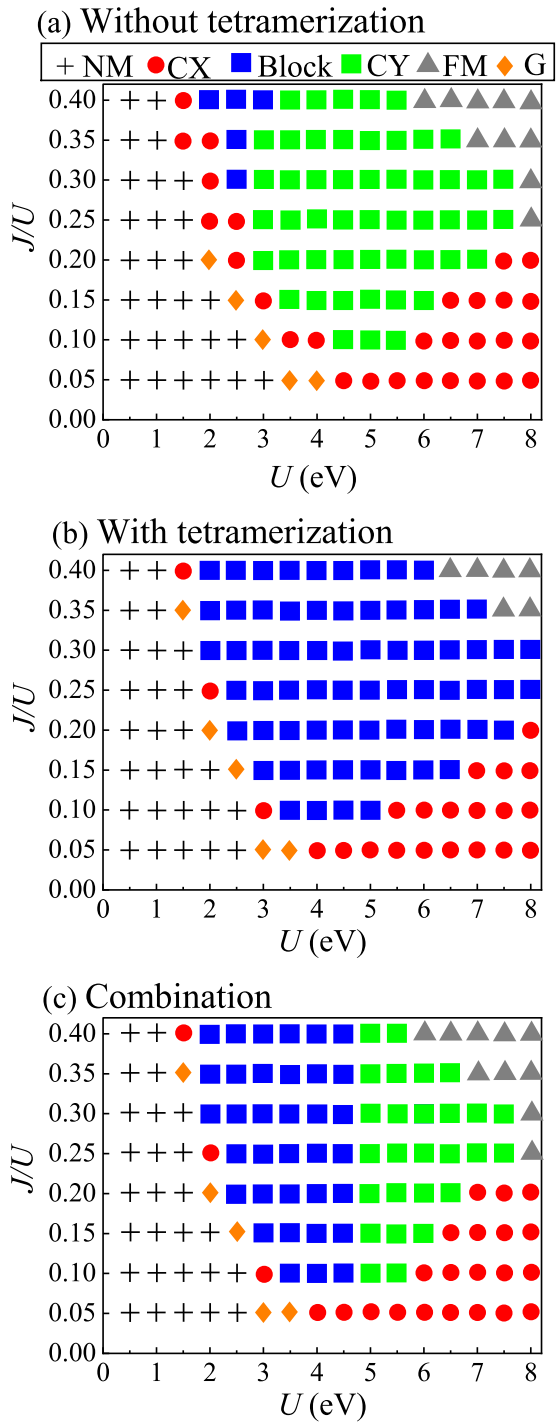

FIG. 4. (a)–(c) Phase diagrams of $BaFe_2Se_3$, employing the LDA + U technique with electronic density $n = 6.0$. (a) Without tetramerization. (b) With tetramerization. (c) Combination, which is the most reliable prediction, obtained by comparing energies with and without tetramerization.

of $BaFe_2Se_3$ is reduced due to intraladder and interladder lattice distortions.

Thus, next we *include* the lattice tetramerization in our calculations [51], where the intraladder Fe-Fe two lattice distances involved are 2.58 and 2.82 Å (for the *Pnma* phase these numbers are much closer, 2.69 and 2.72 Å). In the lattice tetramerization we include the displacements of Se as well, due to the exchange striction magnetostriction of iron. All these distortions are confirmed by both theory and experiment [16,33,38]. By comparing the energies with different magnetic orders, we obtain the new phase diagram shown now in Fig. 4(b). The previously remarked small energy difference favoring CY over block states is now reversed in order, and in the new phase diagram with tetramerization, the CY-type AFM state does not appear in the whole U-J plane. Instead, the block-type state becomes more stable because its energy naturally decreases due to the tetramerization. However, it should be noted that the energies of other magnetic orders increase due to the reduced symmetry. In fact, different magnetic orders have different favorable symmetries. Therefore, it is natural that the phase diagram has changed fairly dramatically by considering the lattice tetramerization.

Comparing the different magnetic states using the same lattice arrangement is incomplete because each particular magnetic order increases its stability, lowers its energy, only with the help of a *particular* lattice distortion. Thus, the best methodology for further progress would be to fully optimize the crystal for each different magnetic order at various values of J and U. However, this is a formidable task. Given the information we have collected thus far, our best path to arrive to our final conclusion is to compare the data of the different magnetic states with and without the lattice tetramerization.

The resulting "combined" phase diagram is presented in Fig. 4(c). The CY-type state with no lattice distortion remains stable in some portions of the phase diagram, while the block state with lattice tetramerization distortion is stable in other regions. The G, CX, and FM states complete the phase diagram. For the widely used ratio $J/U = 0.25$, the qualitative tendency with increasing U is first to form a CX-type AFM in a narrow region, followed by a robust block-type AFM area, and then another robust CY-type AFM region, finally arriving to FM order with further increasing U [52].

The proliferation of many competing states at $n = 6.0$ as compared with $n = 5.5$ probably arises from a combination of correlation effects, increasing Hubbard U and decreasing bandwidth, as well as spin frustrating tendencies between the fully FM state in one extreme and the purely AFM G state (in small regions) in the other, as discussed in previous Hartree-Fock calculations [15]. However, given the information at hand, it can be reasonably assumed that the magnetic state of the $n = 6.0$ Te-based iron ladders, if ever prepared experimentally, will not be the CX-type AFM but more likely either the block- or CY-type arrangements.

C. Projected band structure and density of states

In Fig. 5, we present the "projected" band structure of the nonmagnetic states restricted only to the five iron 3d orbitals corresponding to both $RbFe_2Te_3$ and $BaFe_2S_3$. It is shown that, in general, the band structure is more dispersive from Γ to Z than along other directions, which is compatible with the presence of quasi-one-dimensional ladders along the k_z axis. We also observed that the full bandwidth of the five iron 3d orbitals of $RbFe_2Te_3$ is smaller than for the case of $BaFe_2S_3$, which suggests that the electrons of $RbFe_2Te_3$ are more localized than in $BaFe_2S_3$. More specifically, the maximally

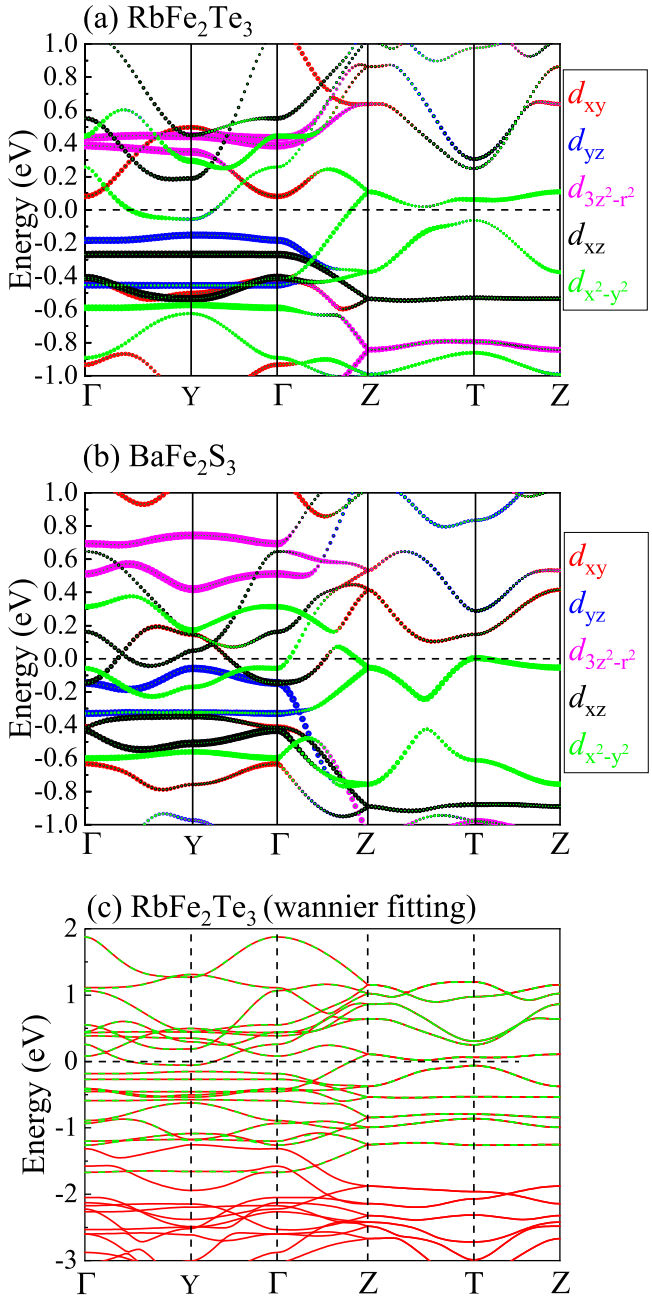

FIG. 5. (a), (b) Projected band structures of $RbFe_2Te_3$ (electronic density $n = 5.5$) and $BaFe_2S_3$ (electronic density $n = 6.0$) for the nonmagnetic (NM) state, respectively. The Fermi level is shown with dashed lines. The weight of each iron orbital is represented by the size of the circle. (c) The original band dispersion is shown by red solid, while the Wannier interpolated band dispersion is shown using green dashed curves for $RbFe_2Te_3$.

localized Wannier functions (MLWFs) were employed to fit the five Fe's $3d$ bands by using the WANNIER90 packages [53]. In these Wannier calculations, the bandwidth of the $3d$ orbitals for $RbFe_2Te_3$ and $BaFe_2S_3$ become approximately 3.56 and 4.06 eV [54], respectively.

In addition, there are 0.5 electrons per Fe less in $RbFe_2Te_3$ than in $BaFe_2S_3$. In $RbFe_2Te_3$, the Fermi surface is mainly contributed by the $d_{x^2-y^2}$ orbital while the contribution of

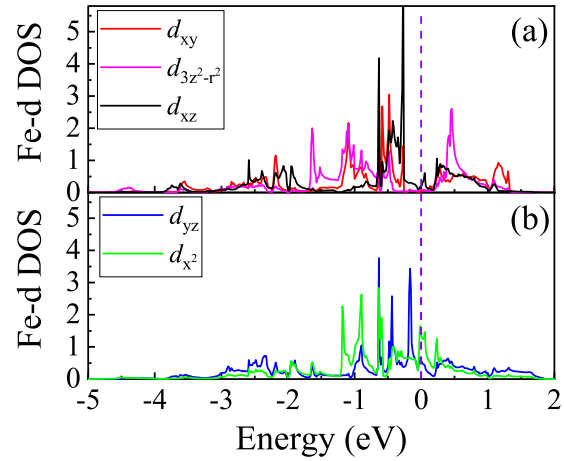

FIG. 6. The projected density of states of the Fe-d orbitals for the nonmagnetic state of $RbFe_2Te_3$ (electronic density $n = 5.5$). The five iron $3d$ orbitals are distinguished by different colors.

the d_{yz} is much reduced, as shown in Fig. 5(a) (note that the apparent green color dominance of the $d_{x^2-y^2}$ bands is misleading: these green bands are actually a mixture of green and blue, the latter arising from d_{yz}). The band crossings at the Fermi level along the Y to Γ and Γ to Z paths have the largest d_{yz} orbital contributions but always heavily hybridized with the $d_{x^2-y^2}$ orbital. For comparison, in $BaFe_2S_3$, the Fermi pockets are mainly contributed by the $d_{x^2-y^2}$, d_{xy}, and d_{xz} orbitals as displayed in Fig. 5(b). This clearly suggests that the Fermi pockets of $RbFe_2Te_3$ are different from $BaFe_2S_3$.

Using the DOS for the Te ladder (Fig. 6), we calculated the relative proportion of the Fermi surface associated with each of the five iron orbitals: 64% are contributed by $d_{x^2-y^2}$ and 26% are from d_{yz}. For this reason, it seems reasonable to assume that $RbFe_2Te_3$ can be described by a two-orbital model or even just one with a combined orbital description ($d_{x^2-y^2}$ hybridized with d_{yz}).

Because with increasing pressure the superconducting phase dome of $n = 6.0$ $BaFe_2S_3$ appears in experiments in the vicinity of the CX-AFM region, the driving force of superconductivity in real systems seems to be the CX spin fluctuations in the nonmagnetic state. According to our previous results for the $n = 5.5$ pressured iron ladders [28], the NM phase can indeed be obtained in theoretical calculations at high pressure. Due to these similarities, it is reasonable to assume that $n = 5.5$ $RbFe_2Te_3$ could also become superconducting at high pressure due to the magnetic similarity with Se- and S-123 ladders, dominated by the CX state, as it was shown in Fig. 3(a).

IV. DISCUSSION

Both experimental and first-principles theoretical results revealed a clear tendency for the bandwidths W of the iron $3d$ orbitals to be enlarged under pressure in $BaFe_2X_3$ [10,38,55], thus enhancing the itinerant nature of the $3d$ iron electrons. Thus, in this respect pressure reduces the electronic correlation strength given by the ratio U/W. To better understand the electronic correlations of $RbFe_2Te_3$, we calculated the "electron localization function" (ELF) [56], quantity widely

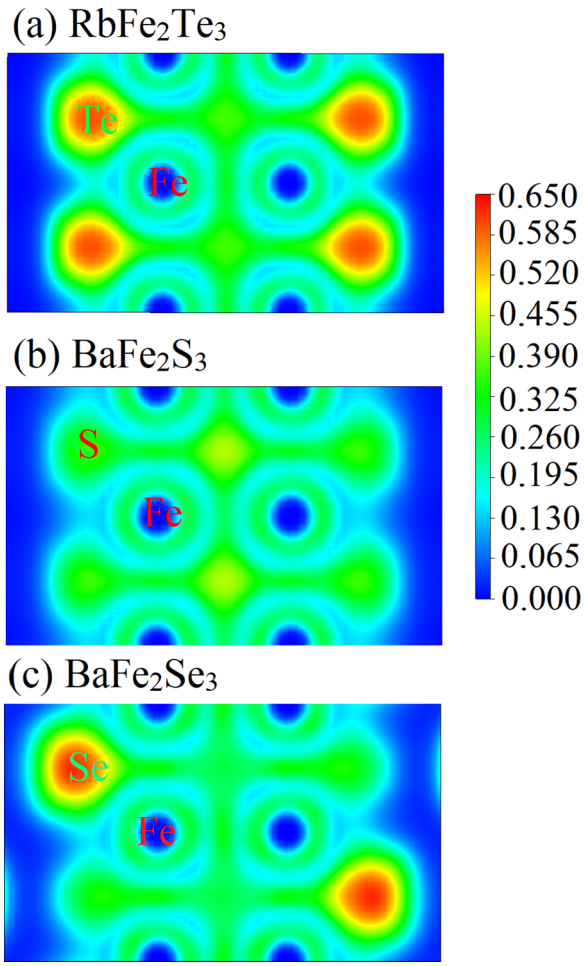

FIG. 7. The calculated electron localization function (ELF) in the iron ladder plane for (a) $n = 5.5$ $RbFe_2Te_3$, (b) $n = 6.0$ $BaFe_2S_3$, and (c) $n = 6.0$ $BaFe_2Se_3$, respectively. To better understand the localization of iron ladders, we set the range of ELF from 0 to 0.65. Generally, ELF=0 indicates no electron localization and ELF=1 indicates full electron localization.

used within *ab initio* methods to characterize the electron localization. As shown in Figs. 7(a) and 7(b), the electrons of $RbFe_2Te_3$ are more localized than in $BaFe_2S_3$, implying that the electronic correlation of Te-based ladders is stronger. More specifically, electrons in Te are more localized than in S, and because Te provides the "bridge" between irons for the electronic mobility, then the net effect is that the tunneling amplitude Fe-Te-Fe is reduced as compared with Fe-S-Fe.

Based on the band structure of the NM state, when compared against $BaFe_2S_3$ (∼4.06 eV) the bandwidth of $BaFe_2Se_3$ (∼3.73 eV) [38] has decreased, which also indicates the electronic correlation effectively is enhanced. This trend was also observed in our previous theoretical study of the magnetic phase [16,38]. Hence, it is reasonable to assume the electronic correlation effects for $n = 6.0$ Te ladders, if they are ever synthesized, would be stronger than in $BaFe_2S_3$ as well. Considering also the block-type AFM order of $BaFe_2Se_3$ that is believed to originate in an orbital-selective Mott state induced by electronic correlations [57–59], it is reasonable to conclude that the ground magnetic state of $n = 6.0$ Te ladders could display similarly interesting properties.

V. CONCLUSION

In this work, the two-leg iron ladder compound $RbFe_2Te_3$, with the iron density $n = 5.5$, was systematically studied using first-principles calculations. The CX-type state was predicted to be the most likely magnetic ground state. The bandwidths of the iron $3d$ bands in the case of $RbFe_2Te_3$ are smaller than in $BaFe_2S_3$.

In addition, the phase diagram of ladders at electronic iron density $n = 6.0$, corresponding to $BaFe_2Se_3$, is found to be much richer than for $n = 5.5$. In particular, the 2×2 magnetic block-type state could be stable at $n = 6.0$ according to DFT phase diagrams, particularly due to lattice tetramerization. Also, the exotic CY state, with AFM rungs and FM legs, which has *not* been observed before neither in experiments nor in calculations, has a large area of stability in the DFT phase diagram at $n = 6.0$.

Moreover, considering the predicted dominance of the magnetic CX state and similarity in electronic structure with other iron ladders, $n = 5.5$ $RbFe_2Te_3$ may become superconducting under high pressure. Also, according to our ELF analysis, the electrons of Te-123 are more localized than in S, implying that the degree of electronic correlation is effectively enhanced for the Te case because the Fe-Te-Fe hopping is reduced. This potential relevance of strong correlation in Te-123 ladders could also induce exotic phenomena, such as the "orbital-selective Mott physics" recently discussed using multiorbital Hubbard models [57–59]. Our overarching conclusion is that experimental studies of iron ladder tellurides are worth pursuing because using Te could lead to interesting results, such as exotic magnetic states and superconductivity under high pressure.

ACKNOWLEDGMENTS

E.D. and A.M. are supported by the U. S. Department of Energy (DOE), Office of Science, Basic Energy Sciences (BES), Materials Sciences and Engineering Division. S.D., Y.Z., and L.F.L. were supported by the National Natural Science Foundation of China (Grants No. 11834002 and No. 11674055). L.F.L. and Y.Z. were supported by the China Scholarship Council. Y.Z. was also supported by the Scientific Research Foundation of Graduate School of Southeast University (Grant No. YBPY1826). Most calculations were carried out at the Advanced Computing Facility (ACF) of the University of Tennessee Knoxville (UTK).

[1] G. R. Stewart, Rev. Mod. Phys. **83**, 1589 (2011).
[2] E. Dagotto, Rev. Mod. Phys. **85**, 849 (2013).
[3] P. C. Dai, Rev. Mod. Phys. **87**, 855 (2015).
[4] P. C. Dai, J. P. Hu, and E. Dagotto, Nat. Phys. **8**, 709 (2012).
[5] I. I. Mazin and M. D. Johannes, Nat. Phys. **5**, 141 (2009).
[6] D. C. Johnston, Adv. Phys. **59**, 803 (2010).

[7] Q. M. Si, R. Yu, and E. Abrahams, Nat. Rev. Mater. **1**, 16017 (2016).

[8] W. Li, H. Ding, P. Deng, K. Chang, C. L. Song, K. He, L. L. Wang, X. C. Ma, J. P. Hu, X. Chen, and Q. K. Xue, Nat. Phys. **8**, 126 (2012).

[9] W. Bao, Q. Z. Huang, G. F. Chen, M. A. Green, D. M. Wang, J. B. He, and Y. M. Qiu, Chin. Phys. Lett. **28**, 086104 (2011).

[10] H. Takahashi, A. Sugimoto, Y. Nambu, T. Yamauchi, Y. Hirata, T. Kawakami, M. Avdeev, K. Matsubayashi, F. Du, C. Kawashima, H. Soeda, S. Nakano, Y. Uwatoko, Y. Ueda, T. J. Sato, and K. Ohgushi, Nat. Mater. **14**, 1008 (2015).

[11] J.-J. Ying, H. C. Lei, C. Petrovic, Y.-M. Xiao, and V.-V. Struzhkin, Phys. Rev. B **95**, 241109(R) (2017).

[12] B. Saparov, S. Calder, B. Sipos, H. B. Cao, S. X. Chi, D. J. Singh, A. D. Christianson, M. D. Lumsden, and A. S. Sefat, Phys. Rev. B **84**, 245132 (2011).

[13] H. Lei, H. Ryu, A. I. Frenkel, and C. Petrovic, Phys. Rev. B **84**, 214511 (2011).

[14] F. Du, K. Ohgushi, Y. Nambu, T. Kawakami, M. Avdeev, Y. Hirata, Y. Watanabe, T. J. Sato, and Y. Ueda, Phys. Rev. B **85**, 214436 (2012).

[15] Q. Luo, A. Nicholson, J. Rincón, S. Liang, J. Riera, G. Alvarez, L. Wang, W. Ku, G. D. Samolyuk, A. Moreo, and E. Dagotto, Phys. Rev. B **87**, 024404 (2013).

[16] S. Dong, J. M. Liu, and E. Dagotto, Phys. Rev. Lett. **113**, 187204 (2014).

[17] M. Mourigal, Shan Wu, M.-B. Stone, J.-R. Neilson, J.-M. Caron, T.-M. McQueen, and C.-L. Broholm, Phys. Rev. Lett. **115**, 047401 (2015).

[18] E. Dagotto, J. Riera, and D. Scalapino, Phys. Rev. B **45**, 5744(R) (1992).

[19] E. Dagotto and T. M. Rice, Science **271**, 618 (1996); see also E. Dagotto, Rep. Prog. Phys. **62**, 1525 (1999).

[20] M. Uehara, T. Nagata, J. Akimitsu, H. Takahashi, N. Mori, and K. Kinoshita, J. Phys. Soc. Jpn. **65**, 2764 (1996).

[21] S. X. Chi, Y. Uwatoko, H. B. Cao, Y. Hirata, K. Hashizume, T. Aoyama, and K. Ohgushi, Phys. Rev. Lett. **117**, 047003 (2016).

[22] T. Yamauchi, Y. Hirata, Y. Ueda, and K. Ohgushi, Phys. Rev. Lett. **115**, 246402 (2015).

[23] M. Wang, M. Yi, S. J. Jin, H. C. Jiang, Y. Song, H. Q. Luo, A. D. Christianson, C. de la Cruz, E. Bourret-Courchesne, D. X. Yao, D. H. Lee, and R. J. Birgeneau, Phys. Rev. B **94**, 041111(R) (2016).

[24] N. D. Patel, A. Nocera, G. Alvarez, A. Moreo, and E. Dagotto, Phys. Rev. B **96**, 024520 (2017).

[25] J. M. Pizarro and E. Bascones, Phys. Rev. Mater. **3**, 014801 (2019).

[26] L. Zheng, B. A. Frandsen, C. Wu, M. Yi, S. Wu, Q. Huang, E. Bourret-Courchesne, G. Simutis, R. Khasanov, D.-X. Yao, M. Wang, and R. J. Birgeneau, Phys. Rev. B **98**, 180402(R) (2018).

[27] E. J. König, A. M. Tsvelik, and P. Coleman, Phys. Rev. B **98**, 184517 (2018).

[28] Y. Zhang, L. F. Lin, J. J. Zhang, E. Dagotto, and S. Dong, Phys. Rev. B **95**, 115154 (2017).

[29] P. Materne, W. Bi, J. Zhao, M. Y. Hu, M. L. Amigó, S. Seiro, S. Aswartham, B. Büchner, and E. E. Alp, Phys. Rev. B **99**, 020505(R) (2019).

[30] N. D. Patel, A. Nocera, G. Alvarez, R. Arita, A. Moreo, and E. Dagotto, Phys. Rev. B **94**, 075119 (2016).

[31] J. M. Caron, J. R. Neilson, D. C. Miller, K. Arpino, A. Llobet, and T. M. McQueen, Phys. Rev. B **85**, 180405(R) (2012).

[32] Y. Nambu, K. Ohgushi, S. Suzuki, F. Du, M. Avdeev, Y. Uwatoko, K. Munakata, H. Fukazawa, S. X. Chi, Y. Ueda, and T. J. Sato, Phys. Rev. B **85**, 064413 (2012).

[33] T. Aoyama, S. Imaizumi, T. Togashi, Y. Sato, K. Hashizume, Y. Nambu, Y. Hirata, M. Matsubara, and K. Ohgushi, Phys. Rev. B **99**, 241109(R) (2019).

[34] K. O. Klepp, W. Sparlinek, and H. Boller, J. Alloy. Compd. **238**, 1 (1996).

[35] G. Kresse and J. Hafner, Phys. Rev. B **47**, 558 (1993).

[36] G. Kresse and J. Furthmüller, Phys. Rev. B **54**, 11169 (1996).

[37] J. P. Perdew, K. Burke, and M. Ernzerhof, Phys. Rev. Lett. **77**, 3865 (1996).

[38] Y. Zhang, L. F. Lin, J. J. Zhang, E. Dagotto, and S. Dong, Phys. Rev. B **97**, 045119 (2018).

[39] M. T. Suzuki, R. Arita, and H. Ikeda, Phys. Rev. B **92**, 085116 (2015).

[40] A. I. Liechtenstein, V. I. Anisimov, and J. Zaanen, Phys. Rev. B **52**, R5467(R) (1995).

[41] V. I. Anisimov, F. Aryasetiawan, and A. I. Liechtenstein, J. Phys.: Condens. Matter **9**, 767 (1997).

[42] V. I. Anisimov, J. Zaanen, and Ole K. Andersen, Phys. Rev. B **44**, 943 (1991).

[43] D. Ootsuki, N. L. Saini, F. Du, Y. Hirata, K. Ohgushi, Y. Ueda, and T. Mizokawa, Phys. Rev. B **91**, 014505 (2015).

[44] J. M. Caron, J. R. Neilson, D. C. Miller, A. Llobet, and T. M. McQueen, Phys. Rev. B **84**, 180409(R) (2011).

[45] Z. S. Gönen, P. Fournier, V. Smolyaninova, R. Greene, F. M. Araujo-Moreira, and B. Eichhorn, Chem. Mater. **12**, 3331 (2000).

[46] Here, we qualitatively obtained the Heisenberg exchange couplings J by comparing the energies of several collinear magnetic orders. Choosing different sets of various magnetic states will result in different values of J. However, it will not change the qualitative tendencies.

[47] L. W. Harriger, H. Q. Luo, M. S. Liu, C. Frost, J. P. Hu, M. R. Norman, and P. C. Dai, Phys. Rev. B **84**, 054544 (2011).

[48] Y. Zhang, L.-F. Lin, J.-J. Zhang, X. Huang, M. An, and S. Dong, Phys. Rev. Mater. **1**, 034406 (2017).

[49] K. Sasmal, B. Lv, B. Lorenz, A. M. Guloy, F. Chen, Y. Y. Xue, and C. W. Chu, Phys. Rev. Lett. **101**, 107007 (2008).

[50] In model calculations, there is a third coupling called U' representing the repulsion between electrons at different orbitals in the same atom. Rotational invariance imposes a constraint $U = U' + 2J_H$ between the onsite same-orbital Hubbard U, the model Hund coupling J_H, and U' [30]. This restricts the range of J_H/U to be less than $\frac{1}{3}$, otherwise if larger than $\frac{1}{3}$ then $U' < J_H$ considered unphysical. Here, we include $J/U > \frac{1}{3}$ for completeness, but none of our physical conclusions change if only $J/U < \frac{1}{3}$ is studied.

[51] Here, the space group of the lattice tetramerization is $Pnm2_1$ (No. 31). To save time, we only consider the (0, 0, 0) coupling between ladders and we use the same use the same structure [$Pnm2_1$ (No. 31)] with different magnetic configurations. However, it should be noted that the magnetic space group is Cc (No. 9) using the same lattice structure plus the block-B AFM $(\pi, \pi, 0)$ which is consistent with [16].

[52] Ferromagnetic tendencies are natural in multiorbital systems with a large Hund coupling as found in [15] using Hartree-Fock

for iron ladders, in one-dimensional t-J systems for spins larger than $\frac{1}{2}$ such as in J. Riera, K. Hallberg, and E. Dagotto, Phys. Rev. Lett. **79**, 713 (1997), and in double-exchange models for manganites.

[53] A. A. Mostofi, J. R. Yates, Y. S. Lee, I. Souza, D. Vanderbilt, and N. Marzari, Comput. Phys. Commun. **178**, 685 (2007).

[54] This value is obtained from our previous calculations of $BaFe_2S_3$, which is consistent with other publication as found in [55].

[55] R. Arita, H. Ikeda, S. Sakai, and M.-To Suzuki, Phys. Rev. B **92**, 054515 (2015).

[56] A. Savin, O. Jepsen, J. Flad, O.-K. Andersen, H. Preuss, and H. G. von Schnering, Angew. Chem. Int. Ed. **31**, 187 (1992).

[57] J. Herbrych, N. Kaushal, A. Nocera, G. Alvarez, A. Moreo, and E. Dagotto, Nat. Commun. **9**, 3736 (2018), and references therein.

[58] N. D. Patel, A. Nocera, G. Alvarez, A. Moreo, S. Johnston, and E. Dagotto, Commun. Phys. **2**, 64 (2019).

[59] J. Herbrych, J. Heverhagen, N. D. Patel, G. Alvarez, M. Daghofer, A. Moreo, and E. Dagotto, Phys. Rev. Lett. **123**, 027203 (2019).